Ice templating water-stable macroporous polysaccharide hydrogels to mimic plant stems

Katsuya KOMIYAMA [1], *Maya ALLARD* [1], *Corentin ESCHENBRENNER* [1], *Clémence SICARD* [2, 3], *Ahmed HAMRAOUI* [1, 4], *Francisco M. FERNANDES* [1]*

[1] Sorbonne Université, UMR 7574, Laboratoire de Chimie de la Matière Condensée de Paris, 75005, Paris, France

[2] Université de Versailles Saint-Quentin-en Yvelines, UMR 8180, L'Institut Lavoisier de Versailles, 78035, Versailles, France

[3] Institut Universitaire de France, Paris

[4] Université Paris Cité, CNRS, UMR8003, Saints Pères Paris Institute for the Neurosciences, 45, rue des Saints-Pères, 75006 Paris, France

Keywords; alginate, cellulose nanocrystals (CNC), macroporous hydrogel, ice-templating, capillary liquid transport

Abstract

Water-stable macroporous hydrogels, inspired by the structural and chemical characteristics of plant stems are expected to open a wide range of possibilities in soft materials for passive liquid transport. However, obtaining efficient materials for these applications still poses a major challenge due to the complexity of shaping hydrogels at the relevant scale-length. Here, water-stable macroporous hydrogels were fabricated using alginate and TEMPO-oxidized cellulose via a new approach involving ice

templating and topotactic ion-crosslinking with Ca^{2+}. This approach allows to fully avoid the energy-intensive lyophilization process and results in composite hydrogels with pore sizes akin to those found in celery xylem, a model we chose for plant stems. Importantly, the pore size could be tailored by adjusting both the ice-growth velocities and the ratios of alginate to oxidized cellulose. The resulting hydrogels displayed remarkable water stability along with viscoelastic properties and wettability that depend on the alginate and oxidized cellulose ratios. Mechanical properties, such as compression stress and toughness, consistently increased with higher alginate contents. In addition, liquid transport measurements on crosslinked hydrogels with varying compositions and ice growth velocities revealed comparable rising speeds to those observed in celery, confirming the ability of polysaccharide-based hydrogels obtained by ice templating and topotactic crosslinking as relevant materials to mimic the function of plant stems.

1. Introduction

In Nature, porous structures play a central role in large array of living organisms [1–4]. Some of the most striking examples come from plant stems, which feature highly sophisticated porous architectures with a high degree of co-alignment. These porous structures constitute the plants' vascular systems—the xylem and the phloem—that are responsible for the capillary liquid transport of water and sap, respectively. Beyond the fundamental understanding of liquid transport in natural materials, plants' vascular systems are a major source of inspiration for a myriad of technological applications. In particular, because of the role of the xylem network in plants, the capacity to mimic its structure, its composition and its function is of technological interest in applications where water transport regulation is required. In the literature, mimicking the xylem

network of plants has led to hydrogels with oriented porosity relevant in a broad range of fields such as tissue engineering [5,6] and drug delivery [7,8]. Numerous fabrication approaches such as micropatterning [9,10], 3D printing [11,12], oriented shear flow [13,14], gravity-induced flow [15], electric field [16], and magnetic field [17] have been proposed to obtain porous anisotropic hydrogels, but these rely on expensive equipment and are applicable only to specific hydrogel compositions.

Recently, ice-templating (also known as freeze-casting or directional freezing) has gained traction for its ability to create hydrogels with hierarchically aligned well-defined pores in a straightforward and inexpensive process [18]. The technique relies on imposing a controlled temperature gradient on a solution or suspension to induce solvent freezing along a specific direction. Solutes, because they are mostly insoluble in ice [19,20], are excluded from the ice fraction and accumulate together with any particle in suspension in the interstitial space formed in between ice crystals. Upon removal of the ice crystals, the process enables the formation of oriented porous materials whose characteristic size can be adjusted by controlling the ice growth velocity. Here, we have implemented this technique to elaborate materials featuring macroporous anisotropic features that mimic the xylem network in plant stems.

Polysaccharides, mainly cellulose and hemicellulose, dominate the chemical composition of plants and are of great interest due to their low toxicity, high biocompatibility, low cost and high abundance. In this regard, mimicking plant structures using polysaccharides exclusively would be an important step to design hydrogels that go beyond the structural features of plant stems. However, only few reports have described the formation of water-stable polysaccharide-based materials with ordered macroporous structure [21–23]. Such limited examples are due to the abundant hydroxyl groups on the backbone of

polysaccharide chains. Most polysaccharides are either soluble in water (*eg.* chitosan, alginate, starch, among others) or readily dispersible in aqueous environment (*eg*. cellulose). This affinity towards water has dramatically reduced their potential use in the context of materials for healthcare or environmental applications, where humid environments prevail. To prevent these shortcomings, we have focused on two polysaccharides that can be stabilized using a similar crosslinking strategy; alginate and oxidized cellulose. Alginate is extracted from a family of brown algae. It is a linear, unbranched polysaccharide consisting of 1,4-linked β-D-mannuronic acid and an α-L-guluronic acid. In presence of multivalent cations such as calcium—among others—ionic crosslinking occurs, resulting in the formation of a hydrogel stabilized by "egg-box" structures (Figure S1) [24]. Cellulose is composed of β-1-4-linked D-anhydroglucose units and is commonly extracted from wood, hemp, cotton, etc. The reaction between cellulose and 2,2,6,6-tetramethylpiperidine-1-oxyl radical (TEMPO) results in the selective oxidation of the hydroxyl groups at the C_6 position on the cellulose surface and induces the formation of carboxylate groups [25] (Figure S2). As with alginate, interaction of the carboxylate groups of cellulose and cations results in stable hydrogels [26,27]. These interactions stand as a key advantage to stabilize multicomponent hydrogels in a single step, leading to increases stability in comparison to single component hydrogels, due to reinforcement effects [28–30]. However, to date this crosslinking method has never been applied for the design of water-stable ice-templated polysaccharide-based hydrogels without an intermediate step requiring the energy-intensive process of lyophilization. The main challenge lies in the need to remove the ice while promoting the stabilization of the freeze concentrated phase. Traditionally this is obtained by lyophilization—the sublimation of ice crystals to obtain a dry foam of solutes.

However, this approach fails in the case where the solutes are water-soluble. To circumvent this limitation—and thus the loss of the macroporous structure, herein, we replaced lyophilization by topotactic stabilization [36]. A strategy our team developed for compositions containing type I collagen, that allows transforming frozen monoliths of biopolymer solutions into macroporous hydrogels without a drying step.

We applied this strategy to dispersions of cellulose nanocrystals (CNC) in alginate solution, to mimic part of the complex architecture and composition of plants' stems. The materials generated by this approach were water-stable and could be designed with pores (50-100 µm in diameter) that exhibit dimensional similarity to the xylem of celery (*Apium graveolens*). The performance of the alginate-CNC ice templated hydrogel as water transport devices were compared with decellularized celery. To untangle the impact of the polysaccharide composition on the morphology, mechanical and water transport properties, the ratio between alginate and oxidized cellulose in the precursor solution/suspension was varied to its widest range. Finally, we demonstrate that the capillary transport properties of alginate-oxidized cellulose hydrogels are mainly dominated by the pore size, suggesting their potential utility in biomedical and environmental applications with an easily tuned macroporosity.

2. Material and Methods

2.1. Materials

Sodium alginate and $CaCl_2 \cdot 2H_2O$ were purchased from Sigma-Aldrich and used without further purification. Cellulose nanocrystals (CNC) were purchased from CelluForce (Canada) and oxidized through TEMPO (2,2,6,6-tetramethylpiperidine-1-oxy radical)-mediated oxidation to obtain oxidized cellulose [31]. Briefly, cellulose nanocrystals (10

g) were suspended in water (1 L) containing TEMPO (0.156 g) and NaBr (2.572 g). A solution of NaClO (12 wt%) was added to the suspension under stirring and the mixture was kept at $pH = 10$ by adding 0.5 M NaOH. The reaction was quenched by adding ethanol (1 mL) and the pH of the mixture was lowered to 7 by adding 0.1 M HCl solution. The mixture was dialyzed for 7 days (Spectra/Por® 4, SpectrumLabs). Finally, the suspension was lyophilized to obtain dry oxidized cellulose powder. The carboxylate content of oxidized cellulose was 1.01 mmol/g based on electrical conductivity titration.

2.2. Plant stem decellularization

Celery (*Apium graveolens*) were purchased at a local supermarket (Paris, France). Decellularization of the celery stem was conducted according to the method reported by Esmaeili et al. [32] (Figure S3). The stem was cut into 1 cm thick transversal sections, immersed in 10% SDS solution, and placed in an orbital shaker at 180 rpm at 25 ˚C for 5 days. After decellularization, samples were washed with distilled water several times and immersed in the solution containing 5 w/v% NaOCl and 3 w/v% NaOH at 25 ˚C for 1 day. Finally, samples were washed with distilled water several times and stored at 4°C until further use.

2.3. Fabrication of ion-crosslinked anisotropic hydrogels

Macroporous hydrogels consisting of alginate and oxidized cellulose were prepared by unidirectional ice-templating method followed by crosslinking with Ca^{2+} (Scheme 1).

The ice-templating setup was composed of a cold finger—a heat conductive aluminum rod partially immersed in liquid nitrogen. Temperature profiles at the top of the cold finger were controlled via a heating resistance controlled by a Proportional–integral–derivative (PID) programmed to ensure a linear progression of the ice front [33]. Alginate-oxidized cellulose relative concentration were set to 7 different ratios with a

144 fixed total solute concentration of 40 g/L (A:C=8:0, 7:1, 6:2, 4:4, 2:6, 1:7 and 0:8, where
145 A and C stand for alginate and oxidized cellulose, respectively) The ratios are shown in
146 Table 1.
147
148 **Table 1.** Composition of the macroporous polysaccharide samples.

Alginate:Oxidized Cellulose (A:C)	**Alginate** / g L^{-1}	**Oxidized Cellulose** / g L^{-1}
8:0	40	0
7:1	35	5
6:2	30	10
4:4	20	20
2:6	10	30
1:7	5	35
0:8	0	40

149
150 For each sample, 2 mL of the suspension were poured inside 12 mm diameter cylindrical
151 molds, placed at the top of the aluminum rod. The bottom of the suspension in the mold
152 was then cooled down from 20 to -80 °C. To explore the impact of the composition on
153 the properties of the obtained hydrogels we have fixed the ice front velocity at 25 µm/s.
154 Conversely, to assess the impact of the ice front velocity on the properties of the hydrogels,
155 we fixed the alginate/oxidized cellulose ratio (A:C=4:4) and applied three different ice-
156 front velocities (10 µm/s, 25 µm/s and 50 µm/s) (Figure S4).
157 After ice templating, all obtained suspensions were crosslinked in 1 M $CaCl_2$ solution for
158 24 hours. To ensure that topotactic crosslinking (melting of the ice crystals with
159 preservation of the porous structure) took place, samples were placed at -3 °C, above the

melting point of $CaCl_2$ solution but below the melting point of pure ice, resulting in self-supported crosslinked hydrogels that do not disperse in the $CaCl_2$ solution [34].

2.4. Morphology of the hydrogels

The hydrogels and the stem of the celery were observed using SEM (S-3400N, Hitachi, Japan) at an accelerating voltage of 10 kV. All samples were coated with a 10 nm layer of gold before observation. After the Ca^{2+} crosslinking, the hydrogels were dehydrated in successive ethanol baths (30, 50, 70, 80, 90, 95 and 100%) followed by supercritical CO_2 drying. When plunged into the ethanol bath, sample A:C=0:8 was rapidly dispersed, preventing its observation by SEM. Images acquired using SEM for the rest of the samples were analyzed with the MorpholibJ plugin [35] in FIJI software [36] to investigate the pore size and distribution. Over 100 pores were counted per SEM image to provide statistically representative values for the pore cross-section areas.

2.5. Rheological characterization

The viscosity of the precursor suspensions with different alginate/oxidized cellulose ratios before crosslinking were determined using a rheometer (MCR 302, Anton Paar, Austria). A 25 mm diameter cone-plate geometry with 1° angle was used. The viscosity measurement was conducted by applying a growing shear-rate from 1 to 500 s^{-1} at 25 °C. The rheological measurements of the different precursor suspensions were carried out after crosslinking with Ca^{2+} ions, using a MCR302 rheometer under a parallel-plate configuration (diameter of 25 mm). The suspensions (1 mL) were introduced onto the bottom plate and crosslinked with 1 mL of 1 M $CaCl_2$ solution 5 minutes before loading the top plate. The frequency sweep was performed from 0.1 to 10 Hz with 1% amplitude at 25 °C.

2.6. Water stability test of ion-crosslinked hydrogels

Water stability tests were carried out on all Ca^{2+}-crosslinked hydrogels, from pure alginate to pure oxidized cellulose. Each hydrogel was immersed in 20 mL of distilled water and stored for 30 days at room temperature. The stability was assessed visually by the sample deformation after this period.

2.7. Mechanical properties of hydrogels

Compression tests of the crosslinked hydrogels were carried out using a rheometer in compression mode (MCR 302, Anton Paar, Austria). The compression speed was set to 1 mm/min and samples were compressed until 60% strain. Samples' dimensions were about 12 mm in diameter and 10 mm in height. A total of 5 replicates were averaged for each sample. Young's modulus was defined from the maximum slope in the low strain regime (0 to 10%). Toughness was determined by the area under the stress-strain curves until 60% stain.

2.8. Wettability

To characterize the wettability of the different crosslinked hydrogels, films with different ratios of alginate and oxidized cellulose were prepared by casting the suspensions on optical microscopy glass slides, with fixed height of 2 mm, using a doctor blade knife. Subsequently, cast suspensions were crosslinked by dipping the slides into 1 M $CaCl_2$ solution at room temperature. The deposited films were peeled off the glass slides with the exception of A:C=1:7 and 0:8 samples, which adhered strongly to the surface of the glass slides and could not be removed. The contact angle formed between the film and water was determined by assessing the interfacial force using the Wilhelmy plate method [34]. During the measurement, a film was suspended from the sample holder, which was connected to an automated microbalance, and partially immersed in distilled water

(Figure S5a). Samples were then vertically pulled from, and then pushed into the water at room temperature at a constant speed rate of 0.05 mm/s (Figure S5b) which results in both receding and advancing contact angles, respectively. The dimensions of the films were 10×5×0.05 mm^3. The contact angles were determined in degrees using the following relation:

$$\theta = cos^{-1}\frac{F_w}{L\sigma} \quad (1)$$

where σ is the surface tension of water ($mN \cdot m^{-1}$), F_w is the wetting force (mN), L is the length of the triple phase line (defined by the film, the air and the water around the sample section) (m) and θ is the contact angle (°).

2.9. Liquid transport

Crosslinked hydrogels with different compositions/ice-growth velocities were used for the liquid transport measurements. Samples were fixed with 2 needles onto a home-built sample holder brought to contact with a 200 ppm methylene blue (MB) solution (lifted progressively by a lab jack until the liquid surface reached the bottom of the sample) (Figure S6a). The progression of the methylene blue in the hydrogels was recorded with video camera (Q-scope QS.20200-P) for 1 hour (Figure S6b) at 16 frames per second. The obtained video footage was analyzed with FIJI software. The surface tension of the methylene blue solution used here was 65 mN/m [37]. A control experiment was performed using single hydrogel walls (prepared as described above by doctor blade casting followed by crosslinking for three different compositions, 2:6, 4:4 and 6:2 A:C). The movement of the dye was monitored as outlined earlier.

3. Results and discussion

3.1. Macroporous alginate-CNC gels obtained by ice templating and topotactic

crosslinking

Ice templating exploits the poor solubility of most solutes in ice, resulting in the formation of two different phases during freezing. One phase is composed of pure ice, and the second corresponds to freeze-concentrated solutes in between the ice crystals. To remove the ice without altering the macroporous structure, we implemented a topotactic stabilization strategy [38]. This technique relies on the concomitant occurrence of ice thawing and polymer crosslinking. Here, we have selected $CaCl_2$ at a concentration of 1 M to induce crosslinking of the alginate-CNC system (Scheme 1).

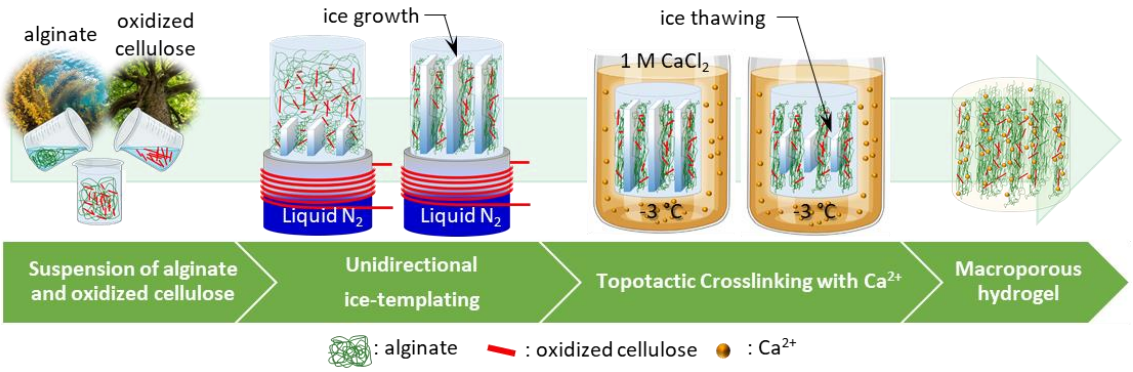

Scheme 1. Schematic illustration of the fabrication process of macroporous anisotropic hydrogels consisting of alginate and oxidized cellulose.

Alginate and oxidized cellulose are crosslinked when exposed to Ca^{2+} ions, leading to the formation of gels. In addition, the presence of $CaCl_2$ at this concentration induces a strong cryoscopic depression (*ca.* -5 °C). Together, these conditions ensure that, when a frozen monolith is placed in a $CaCl_2$ solution, at a temperature between 0 and -5°C, the sample can be progressively transformed into an unfrozen crosslinked hydrogel. We have applied this strategy to the elaboration of macroporous alginate-CNC materials ranging from pure alginate to pure CNC. Regardless of the composition, the resulting materials are fully

self-supported, as can be seen in the left hand side images in Figure 1a-f. The longitudinal sections of the samples, depicted in Figure S7 confirm the pores run parallel to the temperature gradient applied during freezing, regardless of the studied compositions. Notably, pure CNC hydrogel (A:C 0:8) was found unstable in ethanol solution impeding its observation under SEM. While the changes in composition do not affect the macroscopic stability nor the orientation of pores of the obtained hydrogels, SEM observations of the transversal sections of these samples (Figure 1a-f) indicate that the polysaccharide composition does plays a major role in determining the pores' dimensions and morphology.

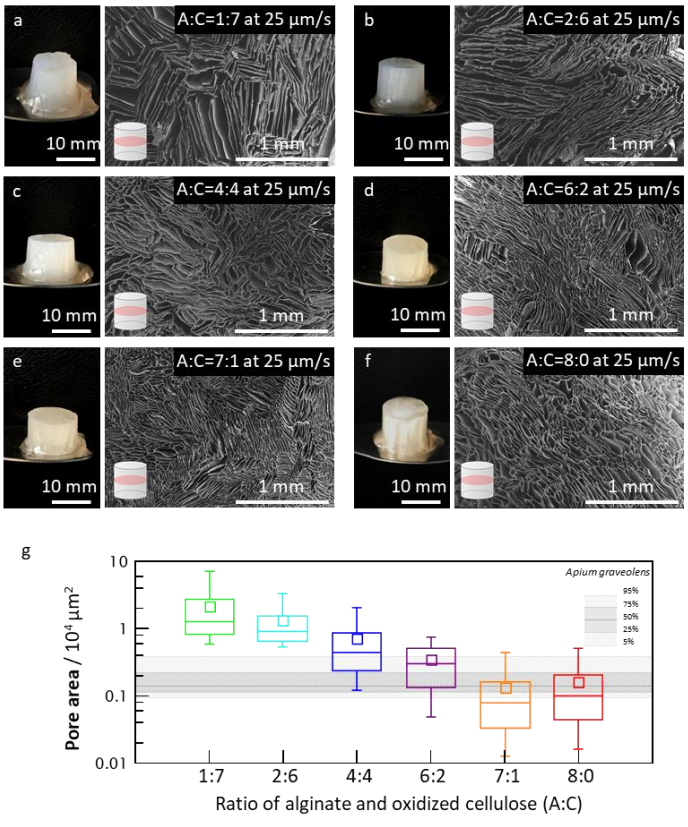

Figure 1. Pictures and SEM images of Ca^{2+}-crosslinked macroporous hydrogels prepared at 25 µm/s (ice growth velocity) using different ratios of alginate and oxidized cellulose. (a) A:C=8:0, (b) A:C=7:1, (c) A:C=6:2, (d) A:C=4:4, (e) A:C=2:6 and (f) A:C=1:7. (g)

Summary of the pore area distribution of alginate and oxidized cellulose macroporous hydrogels at different compositions for 25 μm/s (ice growth velocity). Moustaches delimit the 5 and 95 percentiles of the distribution and box limits represent the 1st and 3rd quartiles. The rectangles and horizontal lines in the boxes represent mean and median values, respectively. Gray horizontal bars depict the pore area distribution of *A. graveolens* xylem vascular system.

Figure 1g depicts the pore area distribution (taken from the area of the pore in the transversal cross-section). Samples exclusively composed of alginate (A:C=8:0) display anisotropic pore section that tend to pack together producing co-alignment (Figure 1a). Increasing the oxidized cellulose content produces larger pores (Figure 1g). The increase in pore dimensions, resulting from increasing CNC content, also results in wider pore size distribution (Figure S8a). In other words, alginate favors smaller and more homogeneous pores with narrower size distribution, whereas CNC promotes bigger, more polydisperse pores.

One of the key factors affecting the growth of ice crystals during ice-templating (and thus determining the final dimensions of the pores in the final materials) is the viscosity of the precursor solution/suspension. We investigated the viscosity of the different compositions of alginate and oxidized cellulose to ascertain their impact on the pore size of mixed polysaccharide hydrogels (Figure S9). The viscosity of the suspensions progressively increased with the ratio of alginate, regardless of the shear rate. This could be associated with the intrinsically low viscosity of oxidized cellulose nanocrystal rods and the relatively high viscosity of entangled alginate chains. In addition, the viscosity of all suspensions showed shear-thinning behavior, which was more pronounced for higher ratios of alginate. This effect could be ascribed to the disentanglement of alginate chain

coils under shear [39], even if strong shear thinning effects have equally been reported for CNCs [40].

The viscosity values determined for the different aqueous suspensions of polysaccharides display an inverse relationship with the pore size. This observation confirms the strong dependence between porosity and viscosity widely discussed in the literature for other compositions [41]. Here, high alginate fractions impose higher viscosity to the polysaccharide solutions/suspension, resulting in restricted lateral growth of ice crystals and consequently smaller and more uniform pore size for the same ice front velocity [42]. However, ascribing the differences in pore size exclusively to the viscosity implies that the different polysaccharides do not have specific interactions with ice during the freezing events.

SEM images in the transversal section of the hydrogels prepared at 4:4 ratio of alginate and oxidized cellulose with different ice-growth velocities (including 10, 25, and 50 µm/s) are shown in Figure 2a to 2c (Figure S10 shows the longitudinal section of those hydrogels). Faster ice-growth velocities induced the formation of smaller pores as reported earlier for other polysaccharides [43]. At 50 µm/s, the ice front velocity yielded pore surface areas of approximately 2.5×10^3 μm^2 (Figure 2c), 16% of the value found for 10 µm/s ($\approx1.6\times10^4$ μm^2, Figure 2a). This effect is due to the creation of more ice nucleation sites on the bottom of the samples as the ice growth velocity increased, leading to smaller macropores [44]. Overall, we found out that the pore size and their respective distributions can be tuned by modulating the alginate/oxidized cellulose relative composition (Figure 1g and Figure S8a), but also by the ice-growth velocities (Figure 2d and Figure S8b). These values (especially those of A:C=6:2 at 25 µm/s and A:C=4:4 at 50 µm/s) are comparable to those measured for the xylem of native celery stems

(≈1.9×10^3 µm^2). In other words, hydrogels reported here, prepared by ice-templating followed by ion-crosslinking, mimic the unidirectional orientation found in plant stems as well as their characteristic dimensions. It is important to note that the biomimetic features of these materials concern not only their structural features, but also their composition, a mixture of polysaccharides close to those found in native plant tissues [45–47].

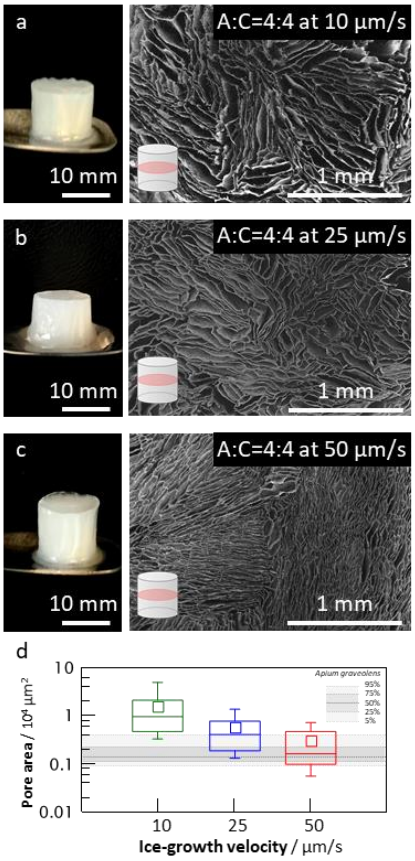

Figure 2. Pictures and SEM images of Ca^{2+}-crosslinked hydrogels prepared at 4:4 ratio of alginate and oxidized cellulose at different ice front velocities. (a) 10 µm/s, (b) 25 µm/s and (c) 50 µm/s. (d) Summary of the pore area distribution of alginate and oxidized cellulose macroporous hydrogels at different ice front velocities. Moustaches delimit the 5 and 95 percentiles of the distribution and box limits represent the 1st and 3rd quartiles. The rectangles and horizontal lines in the boxes represent mean and median values, respectively. Gray horizontal bars depict the pore area distribution of *A. graveolens* xylem

vascular system.

3.2. Characterization of topotactic crosslinked hydrogels

Water stability. The water stability of hydrogels is one of the most significant features for a variety of applications, including biomedical scaffolds, oil extraction/separation, and water purification/desalination [48,49]. To evaluate the contribution of the proportions of alginate and oxidized cellulose on the water stability, topotactic crosslinked hydrogels with 7 different compositions (prepared with an ice-front velocity of 25 µm/s) were immersed in distilled water (Figure 3a) and kept for 30 days at room temperature in static conditions (Figure 3b). At day 30, hydrogels A:C=0:8 were partially dispersed and swollen. On the contrary, all hydrogels containing alginate showed good water stability, suggesting higher alginate contents allow for a more stable crosslinking by calcium ions. These results correlate positively with the higher theoretical crosslinking density for sodium alginate (according to the supplier the carboxyl groups density equals to 5.05 mmol g^{-1} with a M/G ratio of 1.56, which amounts to *c.a.* 2.0 mmol g^{-1} of G units) in comparison with that of oxidized cellulose (carboxyl groups density equal to 1.01 mmol g^{-1}). In general, polysaccharide materials prepared by ice templating redisperse readily in water unless cryogelation occurs [50] or postprocessing steps are added, such as photo-crosslinking or photo-polymerization. [51–56]. Here, we demonstrate that self-supported hydrogels with long term water stability can be achieved via ice-templating followed by ion crosslinking during thawing, without further stabilization by photo-polymerization or photo-crosslinking. Moreover, the components commonly used for the photo-induced gelation rely on particularly harmful components for the environment and are especially difficult to implement in complex, 3D geometries. Ice templating coupled to topotactic

353 stabilization eliminates these bottlenecks in a straightforward and non-toxic process.

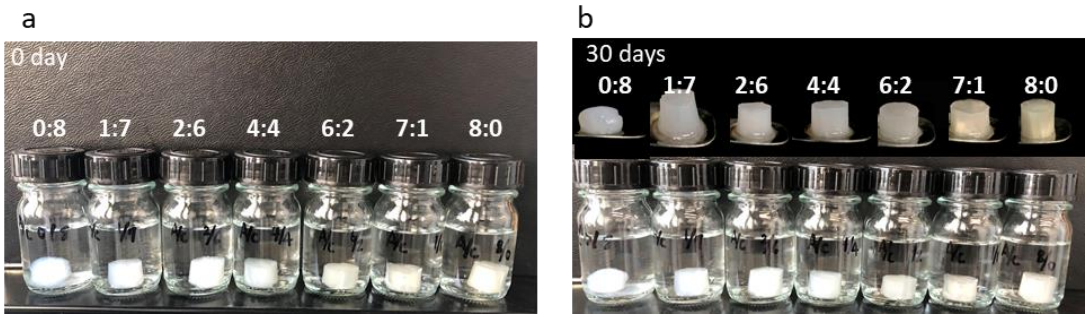

354

355 **Figure 3.** Photos of water stability tests of ion-crosslinked samples with the different ratio
356 of alginate and oxidized cellulose (prepared with an ice growth velocity of 25 μm/s); (a)
357 immediately after the immersion in the water, (b) 30 days after the immersion.

358

359 *Viscoelastic properties* . The viscoelastic properties of hydrogels determine, to a large
360 extent, their applicability for a wide range of uses. To ascertain the viscoelastic properties
361 of the macroporous hydrogels, frequency sweep measurements were carried out on
362 crosslinked suspensions obtained through Ca^{2+}-crosslinking at different alginate/oxidized
363 cellulose components. The storage modulus (G'), loss modulus (G''), and damping factor
364 ($\tan(\delta) = G''/G'$) as functions of frequency are shown in Figure 4a, b, and c. All the
365 compositions of alginate/oxidized cellulose showed a gel-like behavior ($G' > G''$) over
366 the entire angular frequency range. The decrease of tan (δ) with alginate content suggests
367 that in presence of Ca^{2+} ions, this polysaccharide promotes a more solid-like and stiffer
368 internal network to the hydrogels, as previously seen for the water swelling experiments.
369 These observations are equally confirmed by the absolute values of G' and G''. Both
370 values increase with the fraction of alginate, and in both, the values are mostly
371 independent from the angular frequency.
372 The ratio between the two polysaccharides provides a tool to tailor the characteristic pore
373 size and to modulate the crosslinking density inside the hydrogel and, as a consequence,

374 a lever to tune their viscoelastic properties.

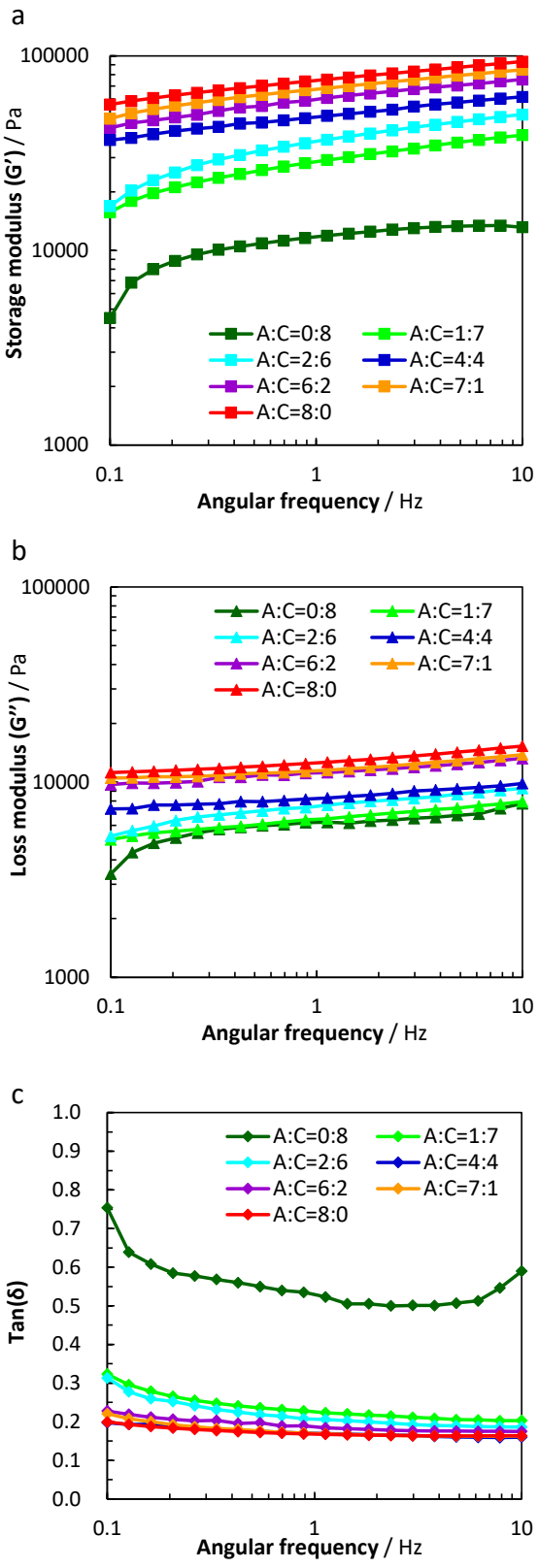

375

Figure 4. Viscoelastic properties of crosslinked gels with different compositions of alginate and oxidized cellulose (prepared with an ice growth velocity of 25 µm/s) (a) storage modulus, (b) loss modulus, and (c) damping factor.

Mechanical properties. To investigate the effects of the composition of alginate and cellulose on the hydrogels, compression tests were performed uniaxially along the freezing direction on macroporous hydrogels prepared from different ratios of alginate/oxidized cellulose with a constant ice growth velocity of 25 µm/s. The resulting stress-strain curves are shown in Figure 5a, and their mechanical properties are described in Table S1. All stress-train curves present an equivalent behavior, with an initial slope corresponding to an elastic deformation regime, followed by a yield point and a plateau, which evolves to reach a densification regime. The compression stress at 60% strain and the yield stress are summarized in Figure 5b, and the Young's modulus and toughness of the hydrogels are summed up in Figure 5c. All measured properties increased with increasing ratio of alginate, with exception for the A:C = 8:0 sample. The A:C=7:1 sample resulted in the highest compression stress, yield stress, and toughness. This optimum value is ascribed to the reinforcement of the alginate hydrogel matrix by low volume fractions of oxidized cellulose, which is likely to favor even dispersion of the filler. At higher volume fractions oxidized cellulose is expected to aggregate and entangle, providing a less effective reinforcement effect. At A:C=7:1 ratio, hydrogels featured an improvement in compression and yield stress up to 107% and 119%, respectively, in comparison to A:C=8:0. Taking into account that this material (A:C=7:1) has the smallest pore area distribution (Figure S8a), it is impossible to ascribe the enhancement of the mechanical properties exclusively to the composite nature of the hydrogels or the rheology of the suspensions, and the size and morphology of the pores should equally be

considered.

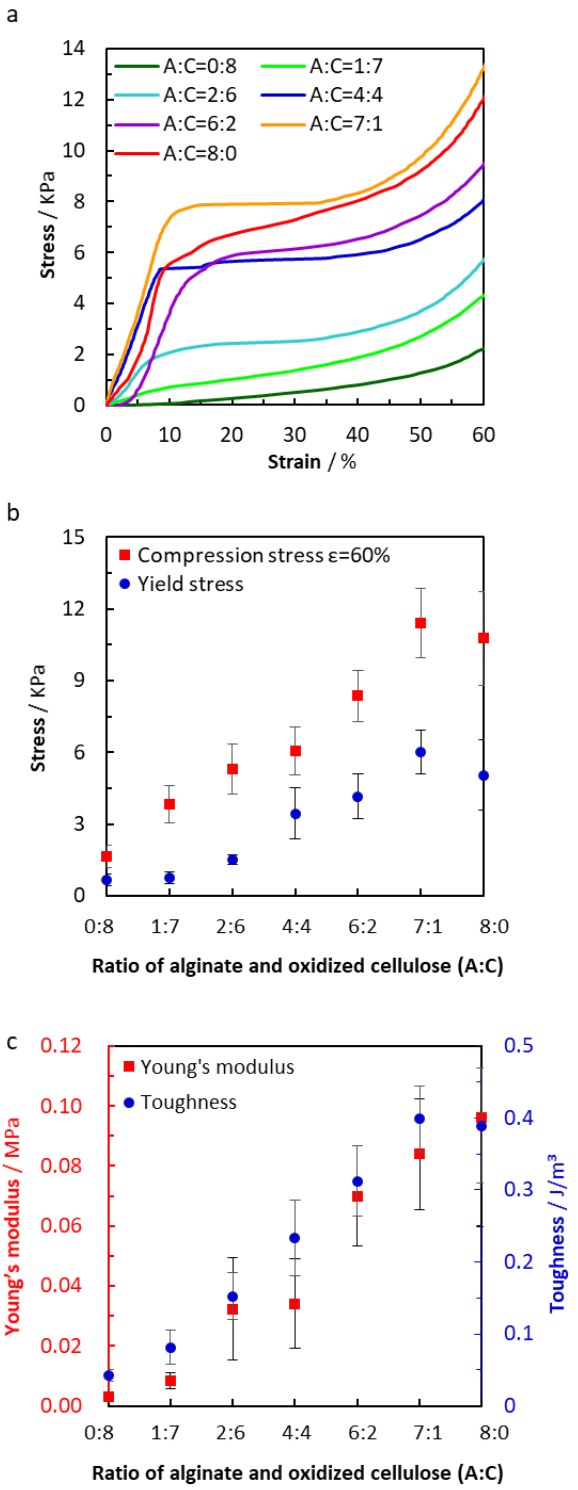

Figure 5. Compression test results of crosslinked hydrogels prepared with an ice growth velocity of 25 μm/s with the different ratios of alginate and oxidized cellulose. (a) Compression strain-stress curves, (b) compression stress at 60% of strain and yield stress,

406 (c) Young's modulus and toughness.

407

408 **3.3. Dynamic contact angle measurement**

409 To assess the wettability dynamics of various hydrogel compositions, we measured the
410 contact angles at the triphase line formed by the films deposited on glass slides, water,
411 and air during dipping and retraction stages (Figure 6). At 38°, A:C=8:0 featured the
412 highest advancing contact angle and it scaled monotonically with the oxidized cellulose
413 contents, reaching 9° for A:C=2:6. This trend is in good agreement with the observations
414 of Montrezor *et al.*, who measured the contact angle for non-crosslinked alginate and
415 oxidized cellulose samples [57]. Although the geometric aspects of these films may differ
416 from the walls inside the hydrogels prepared by ice-templating, their surface chemistry
417 should be strictly comparable. In this sense, the values measured here provide valuable
418 information to describe the wettability of hydrogels of different polysaccharide
419 composition.

420

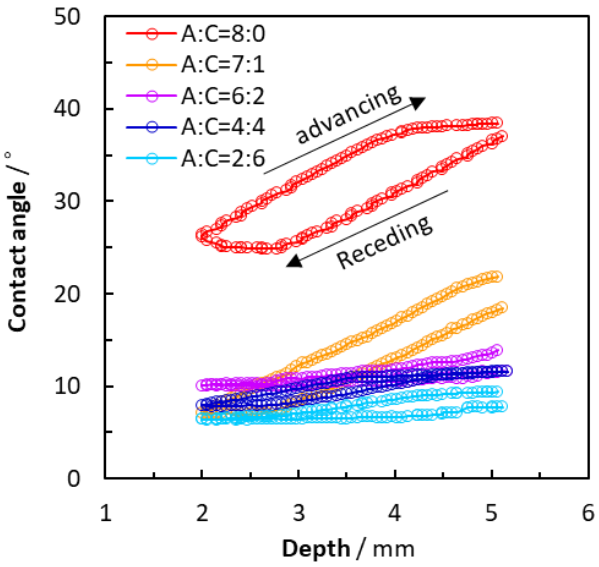

421

422 **Figure 6.** Hysteresis of the dynamic contact angle measurement with deposited films with

423 different ratios of alginate/oxidized cellulose.

424

425 **3.4. Liquid transport measurement**

426 The previous sections have shown that it is possible to control pore size inside the
427 macroporous polysaccharide hydrogels by tuning the ice-growth velocities or the
428 alginate/oxidized cellulose ratio. Furthermore, the wettability measurements demonstrate
429 the influence of composition on the water contact angle. Given the significant roles of
430 pore size and wettability in water transport within biological structures, we have
431 conducted measurements of this property in macroporous polysaccharide hydrogels
432 fabricated through ice templating and topotactic crosslinking. Water transport within
433 cross-linked hydrogels obtained at different ice-growth velocities (10, 25, and 50 µm/s)
434 and different ratios of alginate/oxidized cellulose was measured and compared to the
435 water transport properties found for decellularized stem of celery. To ensure that the
436 experimental setup accurately measured the transport of liquid within the pores, rather
437 than the diffusion of dye through the pore walls, a control experiment was conducted.
438 This involved exposing single polysaccharide walls to the dye (methylene blue, MB)
439 under the same conditions (Figure S11). As no measurable diffusion of the dye in the pore
440 walls was detected within the relevant time frame (60 minutes), we confirmed that all
441 observations of dye progression in the hydrogels corresponded to liquid transport inside
442 the pores.

443 Compositions A:C=6:2, 4:4, and 2:6 were chosen as they reproduce more accurately the
444 global fraction of cellulose in plant stems (approximately 30-80% cellulose) [58,59].
445 Images of liquid transport inside hydrogels—prepared at different ice-growth
446 velocities—up to 60 minutes are shown in Figure 7a and b, respectively. Plotting the

curves of rising height of liquid versus time (Figure 7c and d for different ice-growth velocities and ratios, respectively) shows that the ascending speed through anisotropic hydrogels is faster in the initial stages followed by a slower regime. For a given composition, the rising speed of liquid within the hydrogels prepared at 50 µm/s was the highest and it decreased consistently for samples prepared at slower ice-growth velocities. This observation underscores the significant influence of ice front velocity, and consequently pore size variation, on regulating the liquid transport velocities of the resultant hydrogels, despite their identical compositions.

For hydrogels with different ratios of alginate/oxidized cellulose, the elapsed time before the liquid reached the top of the sample (height = 10 mm) varied with the composition. For sample A:C=6:2 the elapsed time was around 1440 s whereas for sample A:C=4:4 the required time was as high as 3240 s. In addition, in contact with sample A:C=2:6, the liquid did not reach the top of the hydrogel within 60 mins. Although these findings align with the hydrogels' composition and, consequently, the samples' wettability. It is important to highlight that the characteristic contact angles fall within a narrow range, spanning from 9 to 14°. This limited variation hardly accounts for the significant differences observed in transport properties. On the contrary, the pore distribution in the same samples ranges from approximately 3-16×10^3 µm^2, suggesting this parameter plays a predominant role in liquid transport properties. Lower contact angle should translate to a higher capillary coefficient—and thus faster capillary water transport according to Lucas-Washburn equation [60,61]. However, our observations contradict this trend, reinforcing the predominant role of the pores' dimensions and the arrangement of pores in relation to each other in controlling the capillary transport within the macroporous hydrogels reported here.

Celery was used as a native plant tissue reference for comparing the capillary rising behavior of the prepared hydrogels. The decellularized and bleached celery allowed for the visualization of dye rising from the bottom to the top of the celery stem sample (Figure S12a). In living vascular plants, leaves facilitate transpiration. The resulting evaporation generates a vapor pressure depression which promotes capillary liquid transport through the plant stem. However, in this study, liquid was transported up the celery stem without leaves, reaching the top after around 1000 seconds (Figure 7c, d and Figure S12b). Although the celery's initial rising speed was much faster than the prepared hydrogels, it became comparable to hydrogels, especially for A:C=6:2 at 25 μm/s and A:C=4:4 at 50 μm/s. In other words, the hydrogels prepared with alginate and oxidized cellulose via ice-templating in this study successfully mimic both the structural features of plant stems and their liquid transport behavior.

In summary, we successfully created bioinspired hydrogels through ice-templating/ion-crosslinking of alginate and oxidized cellulose suspensions. By adjusting precursor compositions and ice growth velocities, we could control mechanical, surface properties, and morphologies. The resulting hydrogels exhibit capillary water transport behavior primarily dependent on pore size and the alignment of pores in relation to each other. These findings and insights are valuable for developing bioinspired materials resembling native biological tissues, with aligned mechanical properties, for potential biomedical and environmental applications.

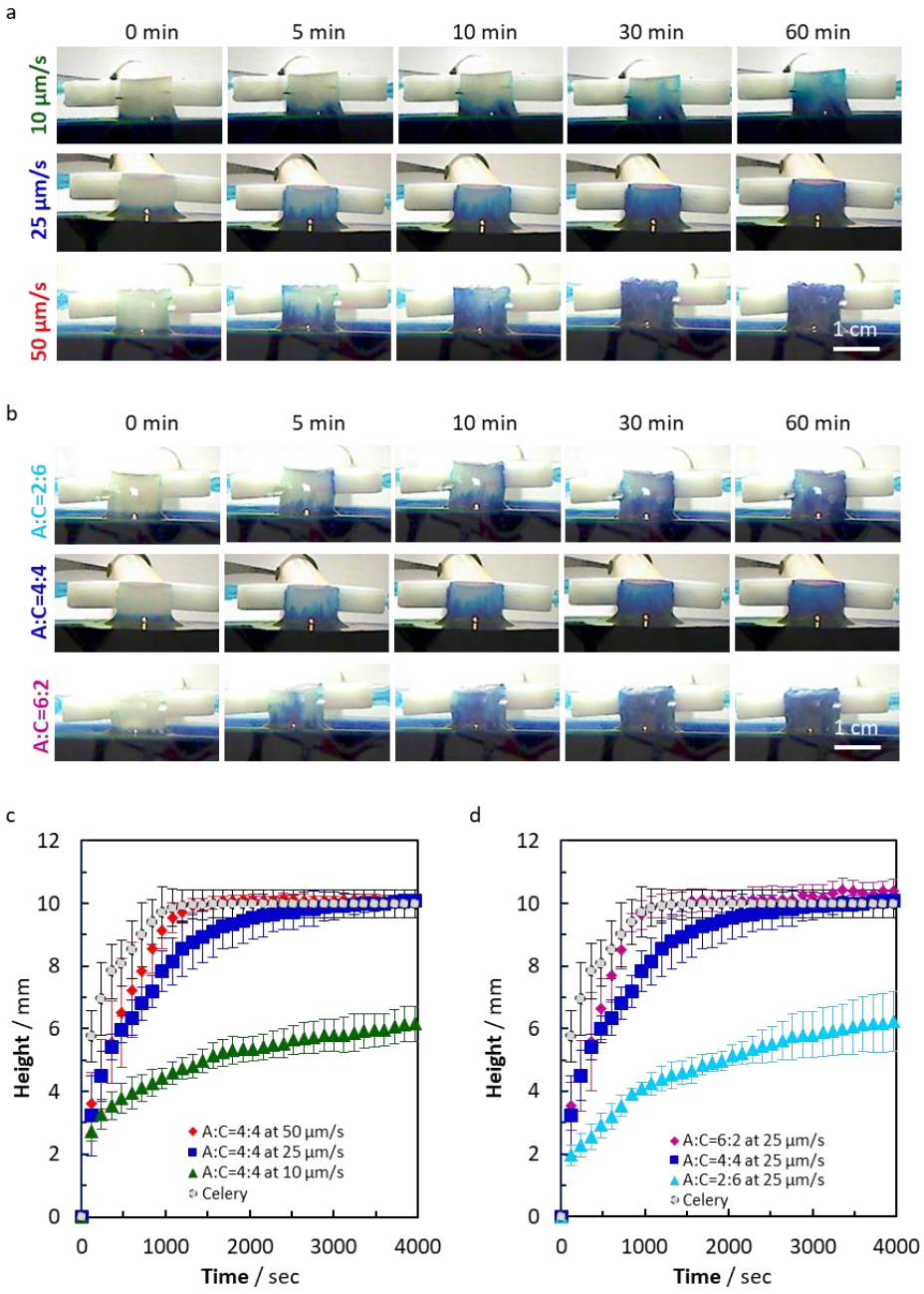

Figure 7. Liquid transport experiment with hydrogels prepared with different compositions of alginate/oxidized cellulose and with different ice-growth velocities, as comparison with celery. Optical photos showing capillary action behavior with the hydrogel prepared at (a) different ice growth velocities (A:C = 4:4) and (b) with different compositions of alginate and oxidized cellulose (ice growth velocity 25 µm/s). (c) Time-liquid height curves with A:C = 4:4 at different ice-growth velocity. (d) Time-liquid height curves with hydrogels obtained by different compositions of alginate and oxidized cellulose with ice growth velocity of 25 µm/s.

In general, porous media can be characterized by studying the kinetics of liquid rise within the pore spaces. Although porous media generally have a complex structure, they can be modeled as a single, vertical capillary or as an assembly of such capillaries. The main difficulties lie in separately estimating the effective mean radius of the capillaries and the contact angle between the liquid and the pore. In the characterization of porous media by capillary rise, the dynamic properties of the liquid front and any meniscus deformation or dynamic contact angle effects will have important consequences. Specifically, we consider that the contact angle between the liquid meniscus and the inner surface of the capillary becomes a dynamic contact angle when the liquid front is in movement as shown in the hysteresis study of the contact angle (Figure 6). It has previously been demonstrated that the resulting time dependence is due to frictional dissipation at the moving wetting front. In modeling the conducted experiments, we employ an analytical expression for height versus time, facilitating the determination of the retardation coefficient. This coefficient encompasses both diffusion and friction contributions to dissipation [56]. Here, we utilize the analytical equation established by Hamraoui *et al.* [57].

$$h(t) = h_e + (h(0) - h_e)\exp\left[-\frac{\gamma\cos(\theta_0)}{\beta_1 h_e}t\right], \text{(E1)}$$

where β_1 is the slowdown coefficient, θ_0 is the equilibrium contact angle, γ surface tension of the used liquid, $h(t = 0)$ and $h_e = h(t \longrightarrow \infty)$ are respectively the initial and the equilibrium heights. In this scenario, the fitting process required only β_1 as a parameter, with the pore radius implicitly incorporated into h_e, which is determined experimentally. The experimental curve fits, presented in Figure 8, were carried out using the analytical expression given in equation (E1). Across all experimental curves, including sample prepared with different composition (A:C=2:6-6:2) of polysaccharide

and with different ice-growth velocities (at 10-50 μm/s), a consistent match with fitting model curves is observed. Table 2 gathers the retardation coefficients calculated for each sample. The retardation coefficients in sample A:C=2:6 at 25 μm/s and A:C=4:4 at 10 μm/s are relatively lower (β_1≈13 and 17 for A:C=2:6 at 25 μm/s and A:C=4:4 at 10 μm/s, respectively), while those for A:C=6:2 at 25 μm/s and A:C=4:4 at 50 μm/s exhibited higher values (β_1≈2.8). This observation aligns well with the experimental data of the liquid height profile, emphasizing the pivotal role of pore size in the liquid transport behavior within the macroporous hydrogels.

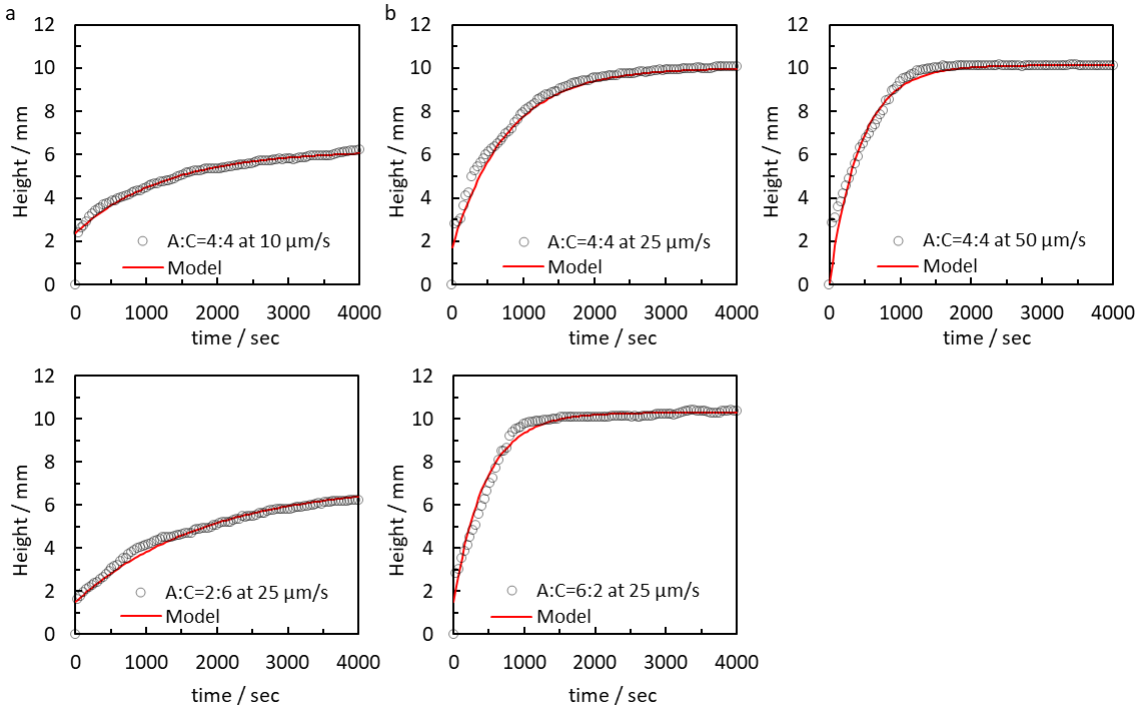

Figure 8. The graphs illustrate the capillary water transport behavior within hydrogels, which were prepared with varying ice-growth velocities (a-c) and distinct compositions of alginate and oxidized cellulose (d and e), along with the theoretical fitting curves as defined by E1.

In the liquid transport behavior within the macroporous hydrogels, diffusion plays a crucial role in governing the initial stages of the liquid transport. This stage is guided by

the pressure gradients generated by the impulsive force, such as the wetting stress. Figure S13a-e displays fitting curves on the experimental $h(t)$ profiles at short times by using diffusion equation $h(t)^2 = 6Dt$, where D denotes diffusion coefficient, and t denotes time. The revealed values of diffusion coefficient highlight a trend where the hydrogels with smaller pore size, such as A:C=4:4 at 10 µm/s and A:C=6:2 at 25 µm/s, yielded higher diffusion coefficients. Figure S13f illustrates the findings, indicating an inverse correlation between the diffusion coefficient and the retardant coefficients. Notably, hydrogels with smaller pore sizes displayed lower retardation coefficients. These variations in the diffusion coefficients among samples indicate that the contribution of the friction at the triple phase line-defined by polysaccharide walls, air, and water—is relatively equivalent for sample A:C=4:4 at 10 µm/s and A:C=2:6 at 25 µm/s but considerably lower than that along a three-phase line of sample A:C=6:2 at 25 µm/s and A:C=4:4 at 50 µm/s.

In summary, this study demonstrates the impact of the intricate correlation between pore size, diffusion coefficients, and retardation coefficients on liquid transport within macroporous hydrogels. It also highlights the central roles of diffusion as the driving force for liquid movement within the pores and friction at the triphase line responsible for the dynamic nature of the contact angle.

Table 2. Retardation coefficients and diffraction coefficients (D) of samples prepared with different ice-growth velocities/compositions of alginate and oxidized cellulose.

Sample	Retardation coefficient	D (mm^2 s^{-2})
A:C=4:4 at 10 µm/s	12.85	0.00072
A:C=4:4 at 25 µm/s	4.91	0.00600

A:C=4:4 at 50 µm/s	2.76	0.01457
A:C=2:6 at 25 µm/s	16.60	0.00103
A:C=6:2 at 25 µm/s	2.78	0.01630

4. Conclusions

Anisotropic macroporous hydrogels, inspired by the structural features of plant stems, were successfully fabricated using alginate and oxidized cellulose through ice-templating followed by topotactic ion-crosslinking with Ca^{2+}, a strategy previously developed in our team to stabilize protein-based biomaterials. The resulting ionic crosslinking rendered the hydrogels insoluble in water. By adjusting the overall amounts of alginate and oxidized cellulose, tunable viscoelastic properties and wettability were achieved, aligning with the respective compositions of alginate and oxidized cellulose. Remarkably, introducing a minimal quantity of oxidized cellulose in the crosslinked hydrogels effectively reinforced the alginate matrix, leading to the highest mechanical properties. Moreover, the morphological characteristics of the hydrogels were tunable, influenced not only by the ice growth speed but also by the composition. These levers allowed to obtain pore sizes comparable with those found in the xylem of celery and, more importantly, to reproduce the plant stems' liquid transport behavior. In fact, capillary liquid transport experiments demonstrated that crosslinked anisotropic hydrogels with smaller pore sizes exhibited faster liquid rising speeds, comparable to those observed in celery. These findings highlight the potential applications of these hydrogels as biomimetic scaffolds in biomedical fields or water purification systems, capitalizing on their anisotropic architecture and their biocompatible composition.

5. Acknowledgement

This work was supported by both the Paris Ile-de France Region - DIM Respore, The French Embassy in Tokyo through Bourses France Excellence and by French state funds managed by the National Research Agency (ANR) through the CellsInFoams project, grant n. ANR-17-CE08-0009

6. Declaration of Competing Interest

The authors declare that they have no known competing financial interests or personal relationships that could have appeared to influence the work reported in this paper.

7. CRediT author statement

Katsuya KOMIYAMA: Investigation, Writing - Original Draft. Maya ALLARD: Investigation. Corentin ESCHENBRENNER: Investigation. Ahmed HAMRAOUI: Investigation. Clémence SICARD: Writing - Review & Editing, Supervision, Funding acquisition. Francisco M. FERNANDES: Conceptualization, Writing - Review & Editing, Supervision, Funding acquisition.

8. References

[1] T.I. Baskin, Anisotropic expansion of the plant cell wall, Annu Rev Cell Dev Biol 21 (2005) 203–222. https://doi.org/10.1146/annurev.cellbio.20.082503.103053.

[2] W. Kong, C. Wang, C. Jia, Y. Kuang, G. Pastel, C. Chen, G. Chen, S. He, H. Huang, J. Zhang, S. Wang, L. Hu, Muscle-Inspired Highly Anisotropic, Strong, Ion-Conductive Hydrogels, Advanced Materials 30 (2018) 1–7. https://doi.org/10.1002/adma.201801934.

[3] P. Calvert, Hydrogels for soft machines, Advanced Materials 21 (2009) 743–756. https://doi.org/10.1002/adma.200800534.

[4] M.J. Hancock, K. Sekeroglu, M.C. Demirel, Bioinspired directional surfaces for adhesion, wetting, and transport, Adv Funct Mater 22 (2012) 2223–2234. https://doi.org/10.1002/adfm.201103017.

[5] J. Radhakrishnan, A. Subramanian, U.M. Krishnan, S. Sethuraman, Injectable and 3D Bioprinted Polysaccharide Hydrogels: From Cartilage to Osteochondral Tissue Engineering, Biomacromolecules 18 (2017) 1–26. https://doi.org/10.1021/acs.biomac.6b01619.

[6] P. Datta, V. Vyas, S. Dhara, A.R. Chowdhury, A. Barui, Anisotropy Properties of Tissues: A Basis for Fabrication of Biomimetic Anisotropic Scaffolds for Tissue Engineering, J Bionic Eng 16 (2019) 842–868. https://doi.org/10.1007/s42235-019-0101-9.

[7] S. Murdan, E lectro-responsive drug delivery from hydrogels, 92 (2003) 1–17.

[8] M.H. Cai, X.Y. Chen, L.Q. Fu, W.L. Du, X. Yang, X.Z. Mou, P.Y. Hu, Design and Development of Hybrid Hydrogels for Biomedical Applications: Recent Trends in Anticancer Drug Delivery and Tissue Engineering, Front Bioeng Biotechnol 9 (2021) 1–18. https://doi.org/10.3389/fbioe.2021.630943.

[9] N. Annabi, K. Tsang, S.M. Mithieux, M. Nikkhah, A. Ameri, A. Khademhosseini, A.S. Weiss, Highly elastic micropatterned hydrogel for engineering functional cardiac tissue, Adv Funct Mater 23 (2013) 4950–4959. https://doi.org/10.1002/adfm.201300570.

[10] M. Nikkhah, N. Eshak, P. Zorlutuna, N. Annabi, M. Castello, K. Kim, A. Dolatshahi-Pirouz, F. Edalat, H. Bae, Y. Yang, A. Khademhosseini, Directed endothelial cell morphogenesis in micropatterned gelatin methacrylate hydrogels, Biomaterials 33 (2012) 9009–9018. https://doi.org/10.1016/j.biomaterials.2012.08.068.

[11] Z. Chen, D. Zhao, B. Liu, G. Nian, X. Li, J. Yin, S. Qu, W. Yang, 3D Printing of Multifunctional Hydrogels, Adv Funct Mater 29 (2019) 1–8. https://doi.org/10.1002/adfm.201900971.

[12] T. Distler, A.R. Boccaccini, 3D printing of electrically conductive hydrogels for tissue engineering and biosensors – A review, Acta Biomater 101 (2020) 1–13. https://doi.org/10.1016/j.actbio.2019.08.044.

[13] M.A. Haque, G. Kamita, T. Kurokawa, K. Tsujii, J.P. Gong, Unidirectional alignment of lamellar bilayer in hydrogel: One-dimensional swelling, anisotropic modulus, and stress/strain tunable structural color, Advanced Materials 22 (2010) 5110–5114. https://doi.org/10.1002/adma.201002509.

[14] X. Ying Lin, Z. Jian Wang, P. Pan, Z. Liang Wu, Q. Zheng, Monodomain hydrogels prepared by shear-induced orientation and subsequent gelation, (2016). https://doi.org/10.1039/c6ra17103f.

[15] J.M. Jang, S.H.T. Tran, S.C. Na, N.L. Jeon, Engineering controllable architecture

in Matrigel for 3D cell alignment, ACS Appl Mater Interfaces 7 (2015) 2183–2188. https://doi.org/10.1021/am508292t.
[16] Q. Lu, S. Bai, Z. Ding, H. Guo, Z. Shao, H. Zhu, D.L. Kaplan, Hydrogel Assembly with Hierarchical Alignment by Balancing Electrostatic Forces, Adv Mater Interfaces 3 (2016) 1–6. https://doi.org/10.1002/admi.201500687.
[17] W. Shi, J. Huang, R. Fang, M. Liu, Imparting Functionality to the Hydrogel by Magnetic-Field-Induced Nano-assembly and Macro-response, ACS Appl Mater Interfaces 12 (2020) 5177–5194. https://doi.org/10.1021/acsami.9b16770.
[18] K. Qin, C. Parisi, F.M. Fernandes, Recent advances in ice templating: From biomimetic composites to cell culture scaffolds and tissue engineering, J Mater Chem B 9 (2021) 889–907. https://doi.org/10.1039/d0tb02506b.
[19] E. Thibert, F. Dominé, Thermodynamics and Kinetics of the Solid Solution of HCl in Ice, J Phys Chem B 101 (1997) 3554–3565. https://doi.org/10.1021/jp962115o.
[20] E. Thibert, F. Dominé, Thermodynamics and Kinetics of the Solid Solution of HNO3 in Ice, J Phys Chem B 102 (1998) 4432–4439. https://doi.org/10.1021/jp980569a.
[21] T. Köhnke, T. Elder, H. Theliander, A.J. Ragauskas, Ice templated and cross-linked xylan/nanocrystalline cellulose hydrogels, Carbohydr Polym 100 (2014) 24–30. https://doi.org/10.1016/j.carbpol.2013.03.060.
[22] K. Yan, F. Xu, S. Li, Y. Li, Y. Chen, D. Wang, Ice-templating of chitosan/agarose porous composite hydrogel with adjustable water-sensitive shape memory property and multi-staged degradation performance, Colloids Surf B Biointerfaces 190 (2020) 110907. https://doi.org/10.1016/j.colsurfb.2020.110907.
[23] S. Christoph, J. Kwiatoszynski, T. Coradin, F.M. Fernandes, Cellularized Cellular Solids via Freeze-Casting, Macromol Biosci 16 (2016) 182–187. https://doi.org/10.1002/mabi.201500319.
[24] P. Sikorski, F. Mo, G. Skjåk-Bræk, B.T. Stokke, Evidence for egg-box-compatible interactions in calcium - Alginate gels from fiber x-ray diffraction, Biomacromolecules 8 (2007) 2098–2103. https://doi.org/10.1021/bm0701503.
[25] A. Isogai, T. Saito, H. Fukuzumi, TEMPO-oxidized cellulose nanofibers, Nanoscale 3 (2011) 71–85. https://doi.org/10.1039/c0nr00583e.
[26] H. Dong, J.F. Snyder, K.S. Williams, J.W. Andzelm, Cation-induced hydrogels of cellulose nanofibrils with tunable moduli, Biomacromolecules 14 (2013) 3338–3345. https://doi.org/10.1021/bm400993f.
[27] N. Masruchin, B.D. Park, V. Causin, I.C. Um, Characteristics of TEMPO-oxidized cellulose fibril-based hydrogels induced by cationic ions and their properties,

Cellulose 22 (2015) 1993–2010. https://doi.org/10.1007/s10570-015-0624-0.
[28] T. Guo, Y. Pei, K. Tang, X. He, J. Huang, F. Wang, Mechanical and drug release properties of alginate beads reinforced with cellulose, J Appl Polym Sci 134 (2017) 44495. https://doi.org/10.1002/APP.44495.
[29] L.F. Wang, S. Shankar, J.W. Rhim, Properties of alginate-based films reinforced with cellulose fibers and cellulose nanowhiskers isolated from mulberry pulp, Food Hydrocoll 63 (2017) 201–208. https://doi.org/10.1016/J.FOODHYD.2016.08.041.
[30] T. Huq, S. Salmieri, A. Khan, R.A. Khan, C. Le Tien, B. Riedl, C. Fraschini, J. Bouchard, J. Uribe-Calderon, M.R. Kamal, M. Lacroix, Nanocrystalline cellulose (NCC) reinforced alginate based biodegradable nanocomposite film, Carbohydr Polym 90 (2012) 1757–1763. https://doi.org/10.1016/j.carbpol.2012.07.065.
[31] T. Saito, A. Isogai, TEMPO-Mediated Oxidation of Native Cellulose. The Effect of Oxidation Conditions on Chemical and Crystal Structures of the Water-Insoluble Fractions, Biomacromolecules 5 (2004) 1983–1989. https://doi.org/10.1021/bm0497769.
[32] J. Esmaeili, S. Jadbabaee, F.M. Far, M.E. Lukolayeh, K.K. Kırboğa, F.S. Rezaei, A. Barati, Decellularized Alstroemeria flower stem modified with chitosan for tissue engineering purposes: A cellulose/chitosan scaffold, Int J Biol Macromol 204 (2022) 321–332. https://doi.org/10.1016/j.ijbiomac.2022.02.019.
[33] C. Stolze, T. Janoschka, U.S. Schubert, F.A. Müller, S. Flauder, Directional Solidification with Constant Ice Front Velocity in the Ice-Templating Process, Adv Eng Mater 18 (2016) 111–120. https://doi.org/10.1002/adem.201500235.
[34] C. Rieu, C. Parisi, G. Mosser, B. Haye, T. Coradin, F.M. Fernandes, L. Trichet, Topotactic Fibrillogenesis of Freeze-Cast Microridged Collagen Scaffolds for 3D Cell Culture, ACS Appl Mater Interfaces 11 (2019) 14672–14683. https://doi.org/10.1021/acsami.9b03219.
[35] D. Legland, I. Arganda-Carreras, P. Andrey, MorphoLibJ: Integrated library and plugins for mathematical morphology with ImageJ, Bioinformatics 32 (2016) 3532–3534. https://doi.org/10.1093/bioinformatics/btw413.
[36] J. Schindelin, I. Arganda-Carreras, E. Frise, V. Kaynig, M. Longair, T. Pietzsch, S. Preibisch, C. Rueden, S. Saalfeld, B. Schmid, J.Y. Tinevez, D.J. White, V. Hartenstein, K. Eliceiri, P. Tomancak, A. Cardona, Fiji: An open-source platform for biological-image analysis, Nat Methods 9 (2012) 676–682. https://doi.org/10.1038/nmeth.2019.
[37] S. Ardizzonea, G. Gabriellib, P. Lazzarib, Adsorption of Methylene Blue at

solid/liquid and water/air interfaces, 1993.
[38] C. Rieu, C. Parisi, G. Mosser, B. Haye, T. Coradin, F.M. Fernandes, L. Trichet, Topotactic Fibrillogenesis of Freeze-Cast Microridged Collagen Scaffolds for 3D Cell Culture, ACS Appl Mater Interfaces 11 (2019) 14672–14683. https://doi.org/10.1021/acsami.9b03219.
[39] C. Rodríguez-Rivero, L. Hilliou, E.M. Martín del Valle, M.A. Galán, Rheological characterization of commercial highly viscous alginate solutions in shear and extensional flows, Rheol Acta 53 (2014) 559–570. https://doi.org/10.1007/S00397-014-0780-4/METRICS.
[40] E.A. Pinto, J.L. Dávila, M.A. d'Ávila, Rheological studies on nanocrystalline cellulose/alginate suspensions, J Mol Liq 277 (2019) 418–423. https://doi.org/10.1016/j.molliq.2018.12.091.
[41] I. Nelson, S.E. Naleway, Intrinsic and extrinsic control of freeze casting, Journal of Materials Research and Technology 8 (2019) 2372–2385. https://doi.org/10.1016/j.jmrt.2018.11.011.
[42] B. Thomas, S. Geng, J. Wei, H. Lycksam, M. Sain, K. Oksman, Ice-Templating of Lignin and Cellulose Nanofiber-Based Carbon Aerogels: Implications for Energy Storage Applications, ACS Appl Nano Mater (2022). https://doi.org/10.1021/ACSANM.2C01033.
[43] S. Christoph, P. Barré, B. Haye, T. Coradin, F.M. Fernandes, Environmentally-stable eco-friendly pectin-silica bio-hybrid foams for soil remediation, Giant 12 (2022) 100119. https://doi.org/10.1016/j.giant.2022.100119.
[44] S. Deville, Ice-templating, freeze casting: Beyond materials processing, J Mater Res 28 (2013) 2202–2219. https://doi.org/10.1557/jmr.2013.105.
[45] J.U. Hernández-Beltrán, I.O. Hernández-De Lira, M.M. Cruz-Santos, A. Saucedo-Luevanos, F. Hernández-Terán, N. Balagurusamy, Insight into pretreatment methods of lignocellulosic biomass to increase biogas yield: Current state, challenges, and opportunities, Applied Sciences (Switzerland) 9 (2019). https://doi.org/10.3390/APP9183721.
[46] K.A. KHALID, A.A. AHMAD, T.L.-K. YONG, Lignin Extraction from Lignocellulosic Biomass Using Sub- and Supercritical Fluid Technology as Precursor for Carbon Fiber Production, Journal of the Japan Institute of Energy 96 (2017) 255–260. https://doi.org/10.3775/JIE.96.255.
[47] P. Ghanney, J.X. Kugbe, D.K. Anning, Role of Microbial Biomechanics in Composting with Special Reference to Lignocellulose Biomass Digestion, Asian J Biotechnol Bioresour Technol (2021) 30–46.

https://doi.org/10.9734/AJB2T/2021/V7I130093.
[48] E.M. Ahmed, Hydrogel: Preparation, characterization, and applications: A review, J Adv Res 6 (2015) 105–121. https://doi.org/10.1016/j.jare.2013.07.006.
[49] X. Zhou, Y. Guo, F. Zhao, G. Yu, Hydrogels as an Emerging Material Platform for Solar Water Purification, Acc Chem Res 52 (2019) 3244–3253. https://doi.org/10.1021/acs.accounts.9b00455.
[50] V.I. Lozinsky, O. Okay, Basic Principles of Cryotropic Gelation, Advances in Polymer Science 263 (2014) 49–101. https://doi.org/10.1007/978-3-319-05846-7_2.
[51] H. Bai, A. Polini, B. Delattre, A.P. Tomsia, Thermoresponsive composite hydrogels with aligned macroporous structure by ice-templated assembly, Chemistry of Materials 25 (2013) 4551–4556. https://doi.org/10.1021/cm4025827.
[52] M. Barrow, H. Zhang, Aligned porous stimuli-responsive hydrogels via directional freezing and frozen UV initiated polymerization, Soft Matter 9 (2013) 2723–2729. https://doi.org/10.1039/c2sm27722k.
[53] J. Wu, Q. Zhao, J. Sun, Q. Zhou, Preparation of poly(ethylene glycol) aligned porous cryogels using a unidirectional freezing technique, Soft Matter 8 (2012) 3620–3626. https://doi.org/10.1039/c2sm07411g.
[54] J. Wu, Y. Lin, J. Sun, Anisotropic volume change of poly(N-isopropylacrylamide)-based hydrogels with an aligned dual-network microstructure, J Mater Chem 22 (2012) 17449–17451. https://doi.org/10.1039/c2jm34010k.
[55] M. Barrow, A. Eltmimi, A. Ahmed, P. Myers, H. Zhang, Frozen polymerization for aligned porous structures with enhanced mechanical stability, conductivity, and as stationary phase for HPLC, J Mater Chem 22 (2012) 11615–11620. https://doi.org/10.1039/c2jm31425h.
[56] M. Chen, J. Zhu, G. Qi, C. He, H. Wang, Anisotropic hydrogels fabricated with directional freezing and radiation-induced polymerization and crosslinking method, Mater Lett 89 (2012) 104–107. https://doi.org/10.1016/j.matlet.2012.08.087.
[57] L.H. Montrezor, L.G.D. Benevenuto, B.F. Antunes, A.C. Amaral, L.P. Novo, A.J.F. Carvalho, E. Trovatti, The influence of chitosan, cellulose and alginate chemical nature on mineral matrix formation, International Journal of Polymeric Materials and Polymeric Biomaterials 71 (2022) 875–885. https://doi.org/10.1080/00914037.2021.1919669.
[58] E.M. Fernandes, R.A. Pires, J.F. Mano, R.L. Reis, Bionanocomposites from lignocellulosic resources: Properties, applications and future trends for their use in the biomedical field, Prog Polym Sci 38 (2013) 1415–1441.

https://doi.org/10.1016/j.progpolymsci.2013.05.013.
[59] I.K. Susheel Kalia, B. S. Kaith, Cellulose Fibers: Bio- and Nano-Polymer Composites, Springer Berlin Heidelberg, 2011. https://doi.org/10.1007/978-3-642-17370-7.
[60] R. Lucas, Ueber das Zeitgesetz des kapillaren Aufstiegs von Flüssigkeiten, Kolloid-Zeitschrift 23 (1918) 15–22. https://doi.org/10.1007/BF01461107.
[61] W. Gardner, Note on the dynamics of capillary flow, Physical Review 18 (1921) 206–209. https://doi.org/10.1103/PhysRev.18.206.

Supporting information

Ice templating water-stable macroporous polysaccharide hydrogels to mimic plant stems

Katsuya KOMIYAMA [1], *Maya ALLARD* [1], *Corentin ESCHENBRENNER* [1], *Clémence SICARD* [2,3], *Ahmed HAMRAOUI* [1,4] *Francisco M. FERNANDES* [1]*

[1] Sorbonne Université, UMR 7574, Laboratoire de Chimie de la Matière Condensée de Paris,
75005, Paris, France
[2] Université de Versailles Saint-Quentin-en Yvelines, UMR 8180, L'Institut Lavoisier de Versailles, 78035, Versailles, France
[3] Institut Universitaire de France
[4] Université Paris Cité, CNRS, UMR8003, Saints Pères Paris Institute for the Neurosciences, 45, rue des Saints-Pères, 75006 Paris, France

* Corresponding author. E-mail: francisco.fernandes@sorbonne-universite.fr; Tel: +33 1 44 27 62 45

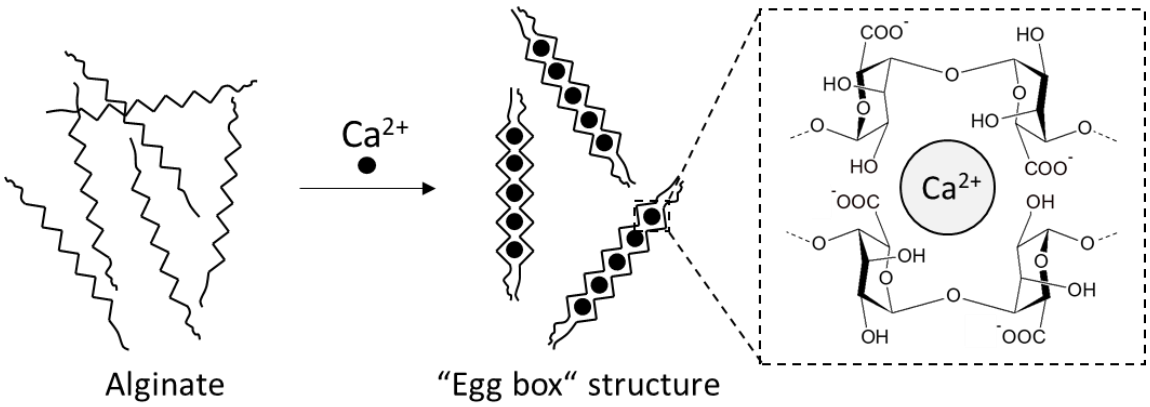

Figure S1. Egg-box structure of alginate gel in the presence of Ca^{2+}.

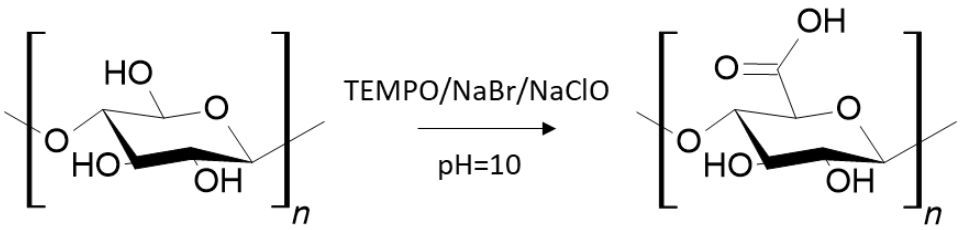

Figure S2. Scheme of TEMPO oxidation of cellulose.

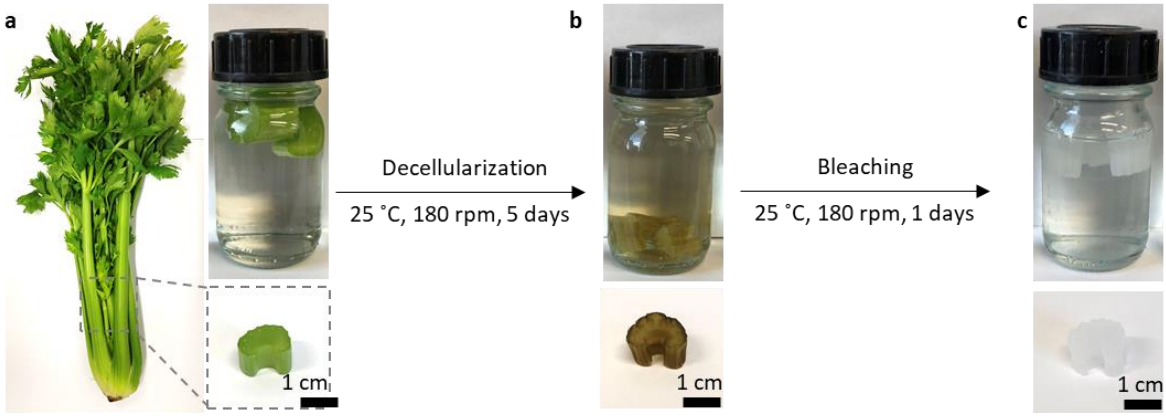

Figure S3. The scheme of the decellularization and bleaching for the celery (*Apium graveolens*), (a) The stem of the celery was cut into 1 cm and then (b) cut samples was

immersed in 10 % SDS solution for 5 days. (c) After 5 days decellularization, samples are immersed in NaClO solution for 1 day for bleaching.

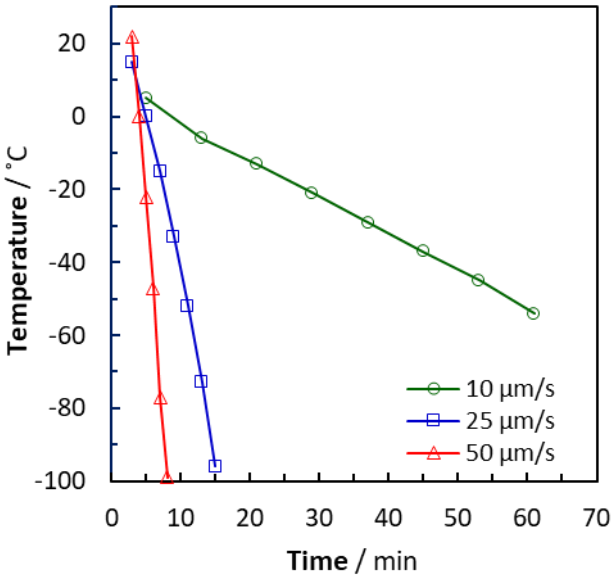

Figure S4. 3 cooling temperature profiles applied in this study for the unidirectional ice-templating, resulting in constant ice-front velocity of 10, 25 and 50 µm/s.

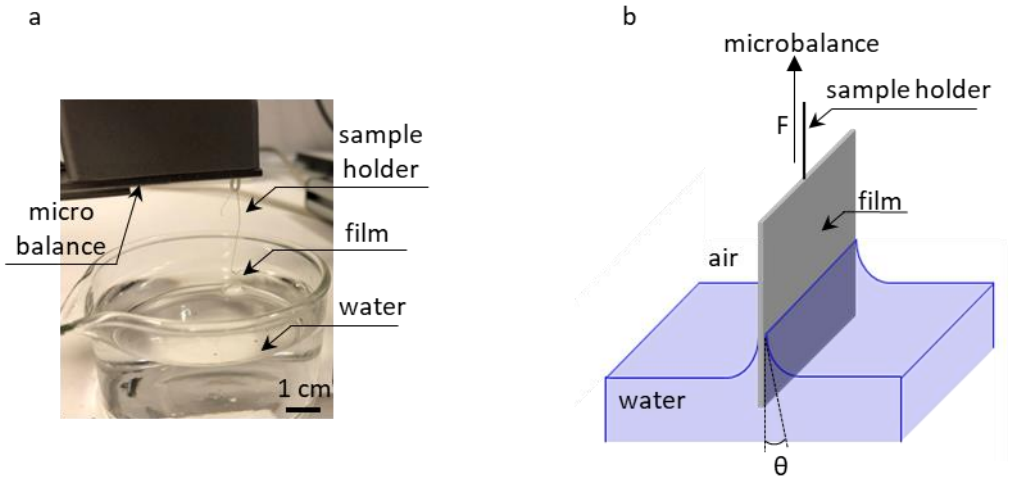

Figure S5. (a) The photo and (b) schematic illustration of the dynamic contact angle measurement with tensiometer.

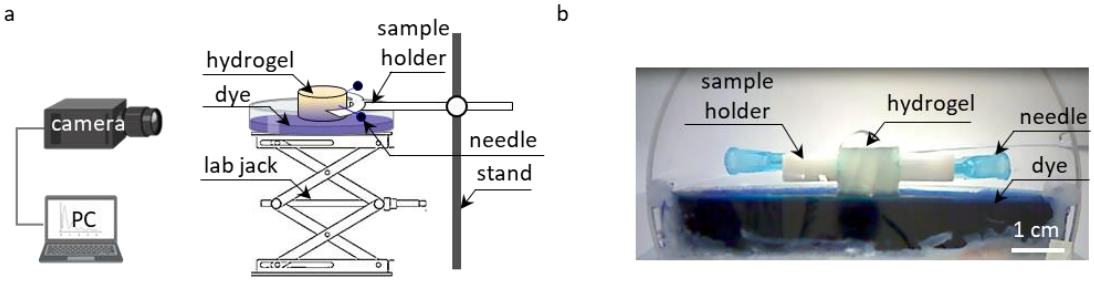

Figure S6. Liquid transport experiment with different composition of alginate and oxidized cellulose and with different ice-growth velocity. (a) Schematic illustration of the liquid transport experimental setup, (b) the photo through the lens of the camera during liquid transport experiment.

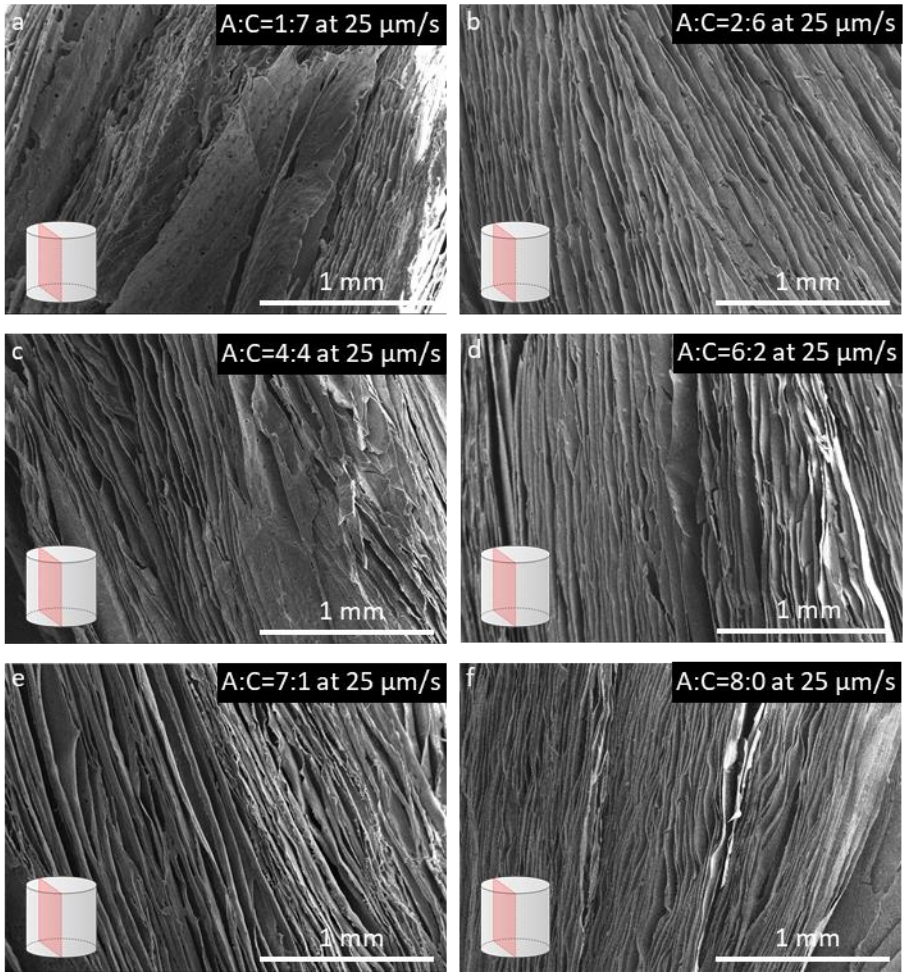

Figure S7. SEM images in longitudinal section of Ca-crosslinked hydrogels with the different ratio of alginate and oxidized cellulose prepared at constant ice growth velocity (25 µm/s). (a) A:C=8:0, (b) A:C=7:1, (c) A:C=6:2, (d) A:C=4:4, (e) A:C=2:6, and (f)

869 A:C=1:7.

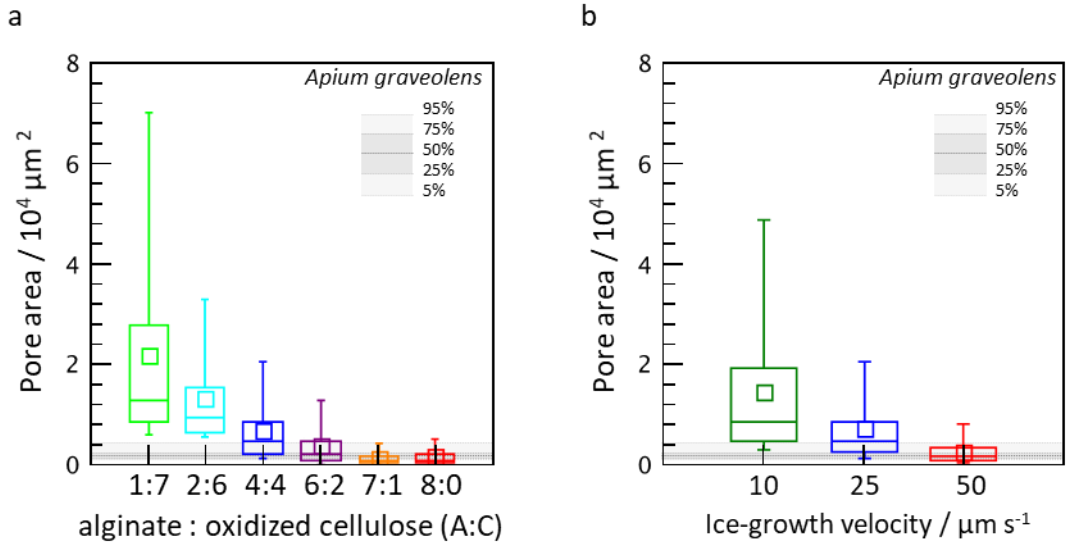

870

871 **Figure S8**. Normal scale pore distribution. (a) Summary of the pore area distribution of
872 alginate and oxidized cellulose macroporous hydrogels at different compositions for 25
873 µm/s (ice growth velocity). (b) Summary of the pore area distribution of alginate and
874 oxidized cellulose macroporous hydrogels (A:C=4:4) at different ice front velocities.
875 Moustaches delimit the 5 and 95 percentiles of the distribution and box limits represent
876 the 1st and 3rd quartiles. Gray horizontal bars depict the pore size distribution of *A.*
877 *graveolens* xylem vascular system.

878

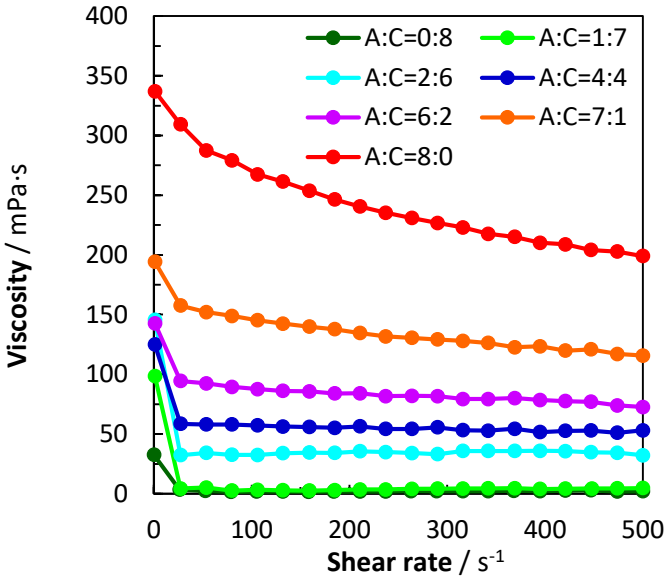

879

880 **Figure S9.** Viscosity profile of the suspensions with different ratio of alginate and

oxidized cellulose.

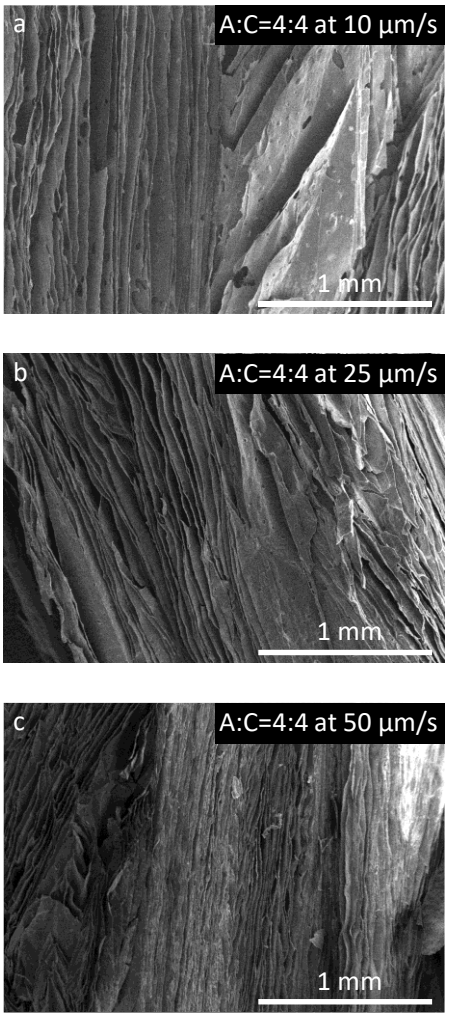

Figure S10. SEM images in longitudinal section of Ca-crosslinked hydrogels prepared at different ice growth velocity (10, 25, and 50 µm/s) at constant ratio of alginate and oxidized cellulose (4:4). (a) v = 10 µm/s, (b) v = 25 µm/s, and (c) v = 50 µm/s.

Table S1. Mechanical properties of hydrogels with an ice growth velocity of 25 μm/s with different compositions of alginate/oxidized cellulose (A:C) after ion-crosslinking.

	Young's modulus / MPa	**Toughness** / J/m^3	**Yield stress** / KPa	**Compression stress** $_{\varepsilon=20\%}$ / KPa	**Compression stress** $_{\varepsilon=40\%}$ / KPa	**Compression stress** $_{\varepsilon=60\%}$ / KPa
0:8	0.003 ± 0.001	0.04 ± 0.01	0.7 ± 0.2	0.3 ± 0.1	0.8 ± 0.2	1.6 ± 0.5
1:7	0.008 ± 0.003	0.08 ± 0.02	0.8 ± 0.3	1.0 ± 0.1	1.8 ± 0.2	3.8 ± 0.8
2:6	0.032 ± 0.017	0.15 ± 0.03	1.5 ± 0.2	2.1 ± 0.4	2.7 ± 0.5	5.3 ± 1.1
4:4	0.034 ± 0.015	0.23 ± 0.05	3.4 ± 1.1	3.9 ± 0.9	4.4 ± 0.8	6.1 ± 1
6:2	0.070 ± 0.017	0.31 ± 0.05	4.1 ± 0.9	5.1 ± 1	5.8 ± 0.9	8.4 ± 1.1
7:1	0.084 ± 0.019	0.40 ± 0.05	6.0 ± 0.9	6.5 ± 0.9	7.3 ± 0.6	11.4 ± 1.5
8:0	0.096 ± 0.036	0.39 ± 0.08	5.0 ± 1.5	5.8 ± 1.3	7.5 ± 1.3	10.8 ± 1.9

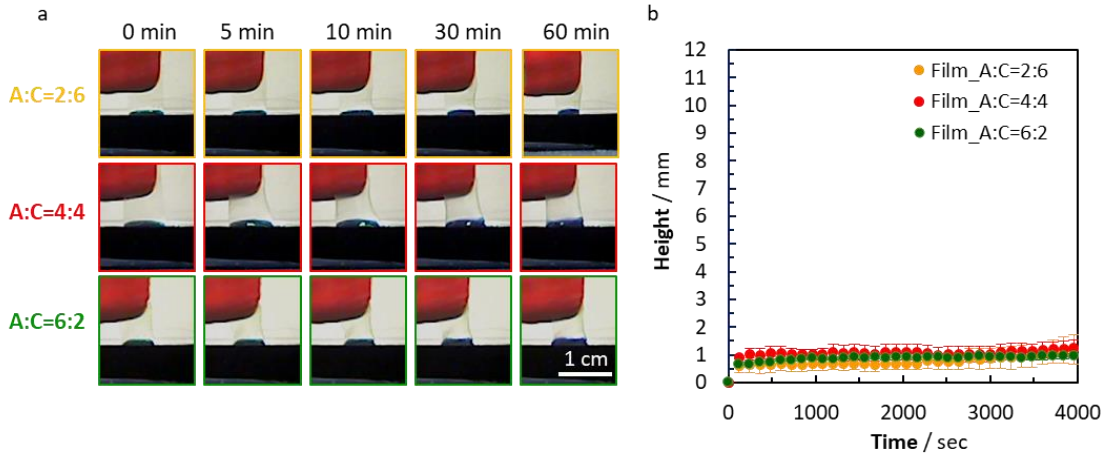

Figure S11. Liquid transport experiment using the films with different compositions of alginate and oxidized cellulose. (a) Optical photos showing capillary action behavior. (b) Time-liquid height curves.

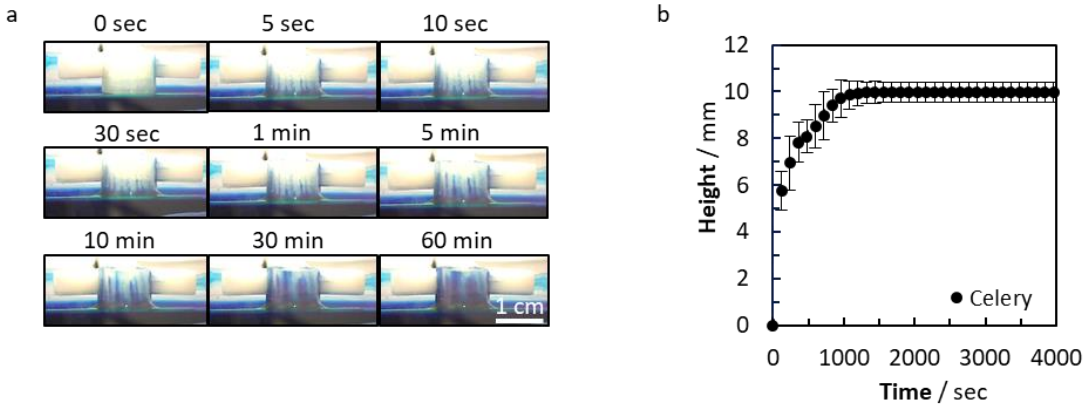

907

908 **Figure S12.** Liquid transport experiment with celery. (a) Optical photos showing capillary
909 action behavior. (b) Time-liquid height curves and rising speeds of celery.

910

911

912

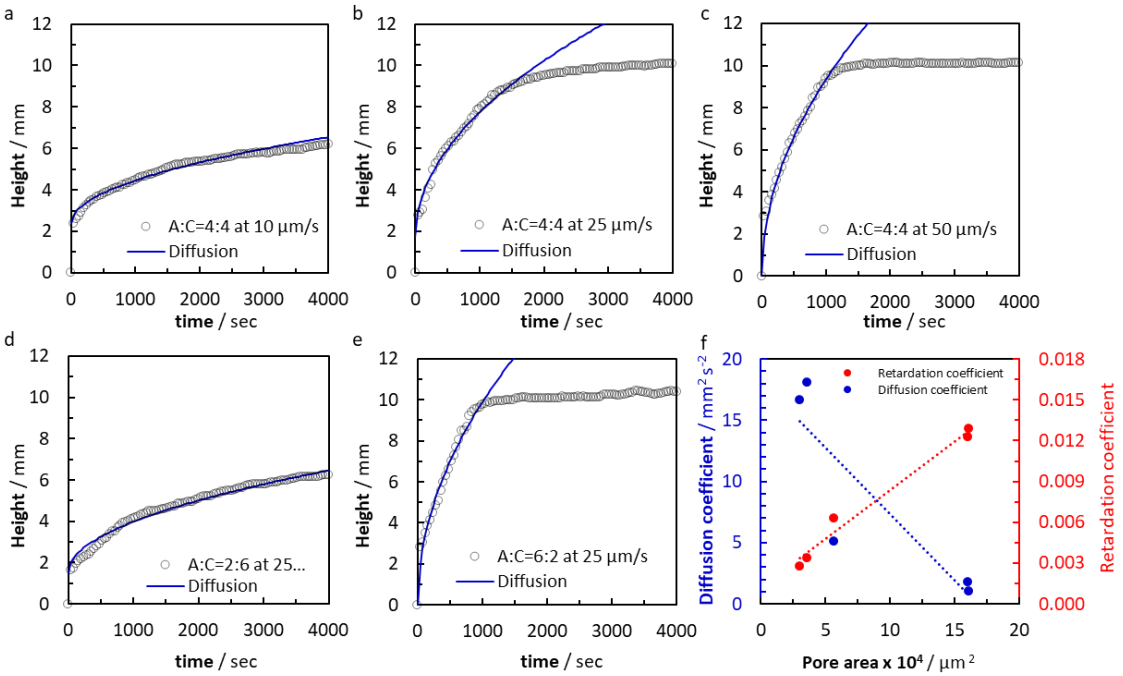

913

914 **Figure S13.** Capillary water transport behavior of hydrogels prepared with different ice-
915 growth velocities (a-c) and different compositions of alginate and oxidized cellulose (d
916 and e) and those theoretical curves fitting to the equation of mean square displacement
917 (i.e. $h(t)^2=6Dt$), (f) trends among pore area, diffusion coefficients, and retardation
918 coefficients. Dashed lines are a guide to the eye.

919